Photoionization of Ca in a static electric field

T. K. Fang,[1,*] J. I. Lo,[2] T. S. Yih,[2] and T. N. Chang[3]

[1]*Department of Physics, Fu Jen Catholic University, Taipei, Taiwan 242, Republic of China*

[2]*Department of Physics, National Central University, Chungli, Taiwan 32001, Republic of China*

[3]*Department of Physics and Astronomy, University of Southern California, Los Angeles, California 90089-0484, USA*

(Received 28 September 2010; published 7 December 2010)

We present a joint theoretical and experimental investigation for electric-field effects on ground-state photoionization of Ca. For an electric field with its direction along the z axis, the dominant field-free, doubly excited, odd-parity (i.e., $3dnp$ and/or $3dnf$) resonances of the $^{1,3}L^o_{J=1}$ (i.e., $^{1,3}P^o_{J=1}$ and $^3D^o_{J=1}$) symmetries are coupled with the even-parity (i.e., $3dns$, $3dnd$, and/or $3dng$) resonances of the $^{1,3}L^e_{J=0}$ (i.e., $^1S^e_{J=0}$ and $^3P^e_{J=0}$) and $^{1,3}L^e_{J=2}$ (i.e., $^3P^e_{J=2}$, $^{1,3}D^e_{J=2}$, and $^3F^e_{J=2}$) symmetries. Using a B-spline-based complex-rotation method with spin-dependent interaction, our theoretically calculated spectrum is found to be in good agreement with the observed spectrum from a cross-beam photoionization experiment for field strengths up to 25 kV/cm. We present in detail a number of qualitative features of the field-induced level crossing and avoided crossing in energy between neighboring resonances, their corresponding changes in width, and the resulting variation in resonance structure profiles. A few "hidden" resonances due to strong overlap with more prominant resonances are also identified theoretically.

DOI: 10.1103/PhysRevA.82.063402 PACS number(s): 32.80.Fb, 32.80.Zb, 32.70.Jz, 31.15.vj

I. INTRODUCTION

A substantial deviation of ionization rates from estimated rates based on the hydrogenic theory for highly excited Stark structures of the Na atom in a static electric field was first reported by Littman *et al.* [1]. This early work was followed by a more comprehensive investigation of the field effect for Rydberg states of one-electron-like alkali-metal atoms by Zimmerman *et al.* [2]. They suggested that the variation in Stark structures could be attributed to the details of level crossing and avoided crossing in the presence of an electric field. Subsequent to another work by Zimmerman *et al.* [3] on the Stark structure of Ba Rydberg states, Gallagher and coworkers [4] showed that the Stark spectra of doubly excited higher angular momentum states of Ba could be described very well by the hydrogenic model of Jacobs *et al.* [5]. Meanwhile, Cooper and coworkers [6] carried out a detailed investigation of the Stark effect near the ionization threshold of rare-gas atoms.

Parallel to the works on Stark spectra for one-electron-like atoms, strong variation of resonance widths and structure profiles of doubly excited autoionization states due to the presence of an electric field was also reported by Freeman and Bjorklund [7] in a three-photon ionization experiment on atomic Sr. In particular, they attributed a dramatic change in the resonance profiles to a sharp avoided crossing between the narrow $4d9f$ and the broad $4d12p$ resonances at approximately 6 kV/cm. In addition, Armstrong and Greene [8] carried out a detailed study to investigate the evolution of the autoionization Stark spectra of excited Ba from the $5d6p\ ^3D^o_1$ initial state as the field strength varies. The result of their R-matrix calculation with a field-dependent frame transformation was in good agreement with the reported experiment data.

More recently, theoretical estimates of electric-field effects were carried out by Fang *et al.* [9,10] using the complex-rotation method for He doubly excited resonances. Detailed calculations were carried out to show the variation of structure profiles for the overlapping doubly excited autoionization series of He [10]. Shortly thereafter, measurement was carried out in the spectral region below the He^+ ($N = 2$) threshold with fields up to 84.4 kV/cm, which led to the observation of more resonance structures than predicted by the theory [11]. To interpret the experimental spectra, Tong and Lin [12] proposed a propensity rule to determine the doubly excited resonances to be preferentially populated. Subsequently, by applying this propensity rule and taking into account the radiative decay of the resonance states, Mihelič and Žitnik [13] carried out a theoretical calculation of He photoionization cross sections, which matched well the spectra observed by Harries *et al.* [11].

Although the spin-orbit interaction is expected to produce only a minor effect for two-electron atoms, Ivanov and Ho [14] studied the combined effect of electric field and spin-orbit interaction on the doubly excited resonances of helium-like ions. Their calculation showed that, under a two-level model, the spin-orbit interaction could manifest itself by modifying the resonance widths of the two resonances when level crossing occurs. Unlike the He atom, for a divalent atom, which has two valence electrons outside a closed-shell ^1S core, the spin-orbit interaction plays an important role in its photoionization spectra, as shown in our recent work on Mg, Ca, and Sr atoms [15,16]. In this article, we present the results of a joint theoretical and experimental investigation of the dc electric-field effect on the ground-state photoionization of Ca. We expect such spectra to reveal in detail not only the mixing due to the spin-orbit interaction, but also the mixing of different J states between the predominant odd-parity resonances of $^{1,3}L^o_{J=1}$ (i.e., $^{1,3}P^o_{J=1}$ and $^3D^o_{J=1}$) symmetries and the even-parity resonances of $^{1,3}L^e_{J=0}$ (i.e., $^1S^e_{J=0}$ and $^3P^e_{J=0}$) and $^{1,3}L^e_{J=2}$ (i.e., $^3P^e_{J=2}$, $^{1,3}D^e_{J=2}$, and $^3F^e_{J=2}$) symmetries. We focus our discussion on the crossing and avoided crossing in energy between overlapping resonances, their corresponding changes in resonance widths, and the variation in resonance

*051420@mail.fju.edu.tw

profiles due to the presence of a static electric field. Section II outlines the theoretical calculation and the experimental procedure. Results and discussion are presented in Sec. III. In particular, we present specific examples to illustrate a number of qualitative features that dictate the contribution from individual resonances (with different S, L, J, and parity) to the total cross section due to the field-induced change in resonance width and scattering phase shift.

II. THEORY AND EXPERIMENT

A. Theoretical calculation

The Hamiltonian for atoms in an external electric field $\vec{F}$ is given by

$$H = H_{\rm nr} + H_{\rm so} + \sum_{i}^{N} \vec{F}\cdot\vec{r}_i, \tag{1}$$

where $H_{\rm nr}$ is the N-electron nonrelativistic Hamiltonian and $H_{\rm so}$ is the spin-orbit interaction as described in [15]. We note that the field strength in Rydberg units is 1 Ry $= 2.57 \times 10^6$ kV/cm.

The Hamiltonian $H_{\rm nr}$ is diagonalized with respect to the zeroth-order-state wave functions $\phi_\mu^\Omega(\theta)$ defined by Eq. (17) of [15], where $\Omega = (SLJM_J)$ represents a set of quantum numbers (i.e., the total spin, the total orbital angular momentum, the total angular momentum, and its corresponding magnetic quantum number, respectively.) Detailed expressions of the Hamiltonian matrix elements for spin-dependent $H_{\rm so}$ are also given in [15].

In a frozen-core Hartree-Fock approximation [17], the matrix element representing the interaction between two J-dependent basis functions coupled by an electric field $\vec{F} = F\hat{z}$ takes the form

$$\left\langle \phi_b^{\Omega_b} \middle| \vec{F}\cdot(\vec{r}_1+\vec{r}_2) \middle| \phi_a^{\Omega_a} \right\rangle = \sum_{j,i} C^{\Omega_b}_{n'_j\ell'_j n_j \ell_j} C^{\Omega_a}_{n'_i\ell'_i n_i \ell_i} \mathcal{F}^{ji}_{ba}, \tag{2}$$

where the matrix $\mathcal{F}^{ji}_{ba}$ is given by

$$\begin{aligned}\mathcal{F}^{ji}_{ba} &= \delta_{S_b S_a} (-1)^{J_b+J_a+L_b+L_a+S_a+\ell_j+\ell'_j-M_{J_b}} F \\ &\times [(2J_b+1)(2J_a+1)(2L_b+1)(2L_a+1)]^{\frac{1}{2}} \\ &\times \begin{pmatrix} J_b & 1 & J_a \\ -M_{J_b} & 0 & M_{J_a} \end{pmatrix} \begin{Bmatrix} L_b & J_b & S_a \\ J_a & L_a & 1 \end{Bmatrix} D^{ji}_{ba},\end{aligned} \tag{3}$$

$$\begin{aligned}D^{ji}_{ba} &= d_{ba}(j'j,i'i) + (-1)^{\Delta_a} d_{ba}(j'j,ii') \\ &+ (-1)^{\Delta_b} d_{ba}(jj',i'i) + (-1)^{\Delta_a+\Delta_b} d_{ba}(jj',ii'),\end{aligned} \tag{4}$$

$$\Delta_a = \ell_{i'} + \ell_i - L_a - S_a, \tag{5}$$

and

$$\Delta_b = \ell_{j'} + \ell_j - L_b - S_b. \tag{6}$$

The matrix element d_{ba} is given explicitly by Eq. (45) of [17].

In a rigorous theoretical calculation, both initial and final states should be obtained by the diagonalization of the Hamiltonian with the electric field included. However, since the initial ground state is approximately a pure $J_I = 0$ state for all electric-field strengths in the present investigation, for simplicity, we have dropped the coupling due to the electric field from our ground-state calculation. As a result, for a linearly polarized light with the direction of polarization parallel to the electric field, only the $M_J = 0$ components of resonant states could be excited from the ground state. Specifically, the field-free final states of the ${}^{1,3}L^o_{J=1}$ symmetries (i.e., ${}^{1,3}P^o_{J=1}$ and ${}^3D^o_{J=1}$) are coupled with those states of ${}^{1,3}L^e_{J=0}$ (i.e., ${}^1S^e_{J=0}$ and ${}^3P^e_{J=0}$) and ${}^{1,3}L^e_{J=2}$ (i.e., ${}^3P^e_{J=2}$, ${}^{1,3}D^e_{J=2}$, and ${}^3F^e_{J=2}$) symmetries by the external electric feld for the $M_J = 0$ components.

The photoionization cross section $\sigma(E)$ from the initial ground state $\Phi_I^{J_I M_{J_I}}$ with an energy E_I is obtained by calculating the dynamic polarizability following the procedure detailed in [15], except that the final state Φ_μ^{JM} in Eq. (23) of [15] should be replaced by

$$\Phi_\mu(\theta) = \delta_{M_J 0} \sum_{\rm SLJ\nu} C_\nu^{({\rm SLJ})\mu} \phi_\nu^\Omega(\theta), \tag{7}$$

with a sum over all J states due to Stark mixing. The B-spline-based complex-rotation method (BSCR) approach also offers the possibility to analyze in detail the theoretical cross section $\sigma(E)$ in terms of the contribution from individual resonance following the procedure outlined in [10].

B. Experimental procedure

The experimental setup consists of the incident light, the interaction zone, the detecting system, and the atom gun system. Figure 1 presents a schematic diagram of the interaction zone and the detecting system. The synchrotron light with fixed polarization direction from the Seya beam line at the National Synchrotron Radiation Research Center (NSRRC) in Taiwan, in the spectral region of 1500 to 2100 Å, enters the interaction zone through a LiF window, which separates the monochromator and the experimental chamber and protects the monochromator from contamination by the metal vapor. The sodium-salycilate-coated glass, on the opposite side, was used to transfer transmitted VUV photons into visible fluorescence, which are detected by a photomultiplier (PMT). The slit width was adjusted to about 200 μm with a monochromator grating of 1200 G/mm to provide sufficient photon flux at about 5×10^{10} photons/s in the interaction zone.

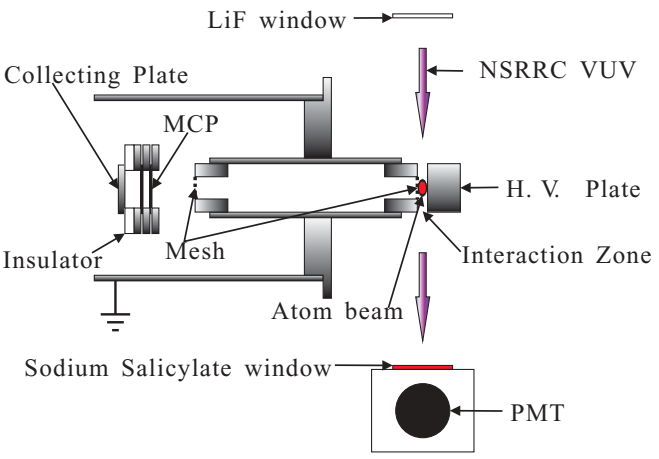

FIG. 1. (Color online) Schematic diagram of the interaction zone and the detecting system.

The observed spectrum was obtained with scan steps that vary at will from 0.06 to 0.6 Å. The resolving power of the beam line is about 1000, or at an energy resolution of about 1.6 Å. Although the energy resolution of the sychrotron radiation is not as good as that for the multiphoton laser experiments, it nevertheless could cover a much broader spectral region in a single experiment. This offers the opportunity to study in detail the onset of the strong variation of Stark profiles as the field strength increases.

A uniform dc electric field of approximately 3% stability was generated near the center of two parallel stainless-steel circular plates with an outer diameter of 30 mm. An atomic beam was injected into the interaction region in a direction perpendicular to the VUV light and the electric field was aligned in the same direction as the polarization of the incident light. On the right side was a solid high-voltage plate. On the left was a hollow plate, wired to the ground, with a central hole of inner diameter 15 mm. A tungsten mesh was placed on the surface of the hollow plate to sustain a uniform electric field in the interaction region. It allowed ions to reach the ion detector on the left. A similar hollow plate with mesh was placed in front of the ion detector to prevent electric-field penetration and to protect the Chevron-type microchannel plate (MCP) from damage due to the high field.

Figure 2 presents the layout of the atom gun system. The atom gun was designed to consist of two parts, that is, a beam-defining nozzle 12 cm long with a 1×2-mm cross section at the top and a metal reservoir at the bottom. Two heaters were used to heat each part separately to the desired specific temperature up to 1200°C. The heating element is made of tungsten filament and it is wired around the reservoir tube with a fixture to avoid direct contact between the filament and the stainless reservoir. The atom gun was heated by the radiation heat of the filament, which is substantially hotter than the atom gun itself. Temperature controllers were used to control the gun system to a set of stabilized temperatures, which allow the atom gun to generate a steady beam flux for different metals. For Ca, the filament temperatures were set at 900°C for the upper one and 850°C for the lower one.

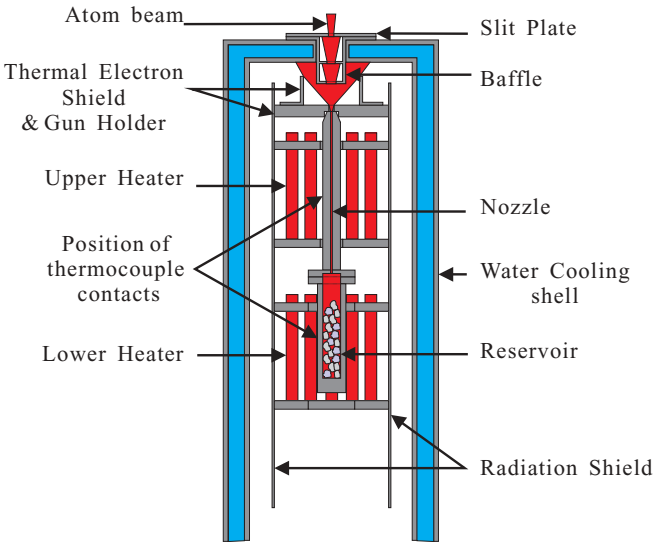

FIG. 2. (Color online) Schematic diagram of the atom gun system.

The high temperature of the tungsten filament emits a large number of thermal electrons, which has a sufficiently high energy to ionize the metal vapor ejected from the atom gun. Consequently, there must be a shield to prevent thermal electrons from colliding with neutral atoms on their way to the interaction zone. In addition, any metal condensation on the electrodes may cause electric breakdown and fail to sustain the electric field strength. A carefully designed baffle was installed at the top of the system to minimize the metal condensation on the electrodes and, at the same time, to inject metal vapor into the interaction zone in the direction perpendicular to the electric field.

The relative positions among the atom gun, baffle, and electrodes must be adjusted with great care to prevent the contamination of electrodes and the spread of thermal electrons. The baffle is put on the top of the water cooling shell surrounding the heating element as shown in Fig. 2. It consists of two baffle plates below a slit plate. Its total length is 44 mm. There is one central hole on each baffle plate. The lower baffle plate, with a hole of 10-mm diameter, and the upper plate, with a hole of 6.5-mm diameter, are designed to optimize the condensation rate on the electrodes. A slit plate with a 1×10-mm rectangular aperture is placed on the top of this baffle. The distance from the slit plate to the center of electrode plates is 30 mm. Contact between the cooling shell and the slit plate warrants a low temperature of the slit plate and assures that Ca atoms from the atom gun are in the ground state. The distance from the bottom side of the baffle to the top of the gun nozzle is 30 mm. The entire system is made of stainless steel except for the tungsten filament.

III. RESULTS AND DISCUSSION

We first discuss qualitatively the change in resonance widths and the resulting variation in structure profiles due to the crossing or avoided crossing in energy of neighboring resonances as the field strength F increases. We start from a two-level approximation similar to the one presented by Ivanov and Ho in [14]. For a complex Hamiltonian, the energy difference between two resonances is given by

$$E_1(F) - E_2(F) = \delta E(F) - i\delta\Gamma(F) = \sqrt{A} = \sqrt{(E_a - E_b)^2 + c(F)}, \quad (8)$$

where E_a and E_b are the complex energies of the unperturbed resonances and $c(F) = 4V_{ab}V_{ba}$. The complex matrix $V_{ab}(F)$ represents the field-dependent interaction between the two resonances. For an actual crossing to occur at a field strength $F = F_0$, either the real part or the imaginary part (but not both) of the energy difference $E_1 - E_2$ equals 0, that is, a crossing in energy if $\delta E(F_o) = 0$ or a crossing in width if $\delta\Gamma(F_o) = 0$. Near the crossing, that is, when the field strength F approaches F_o, the difference between unperturbed complex energy eigenvalues, that is, $E_a - E_b$, could be expanded as

$$E_a - E_b \simeq a(F - F_o) + \left(\Delta E - i\frac{\Delta\Gamma}{2}\right), \quad (9)$$

where $\Delta E - i\frac{\Delta\Gamma}{2}$ is the difference between the unperturbed energies $E_a - E_b$ at $F = F_o$ and $a = a_R + ia_I$ is a complex coefficient, with a_R and a_I representing the rates of change of

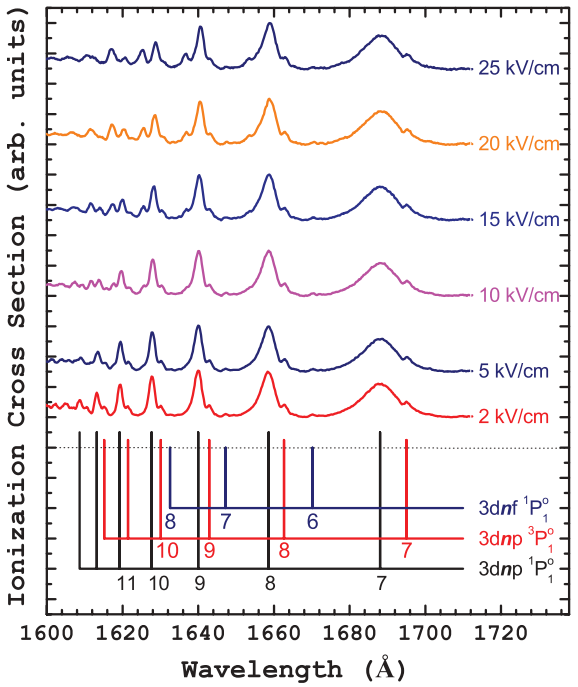

FIG. 3. (Color online) Observed Stark spectra with a field strength of up to 25 kV/cm.

$E_a - E_b$ as F approaches F_o near the crossing. Qualitatively, for a crossing in energy, a_R dominates over a_I, since, near the crossing, the rate of change in energy is greater than the rate of change in width. Similarly, for a crossing in width, a_I dominates over a_R.

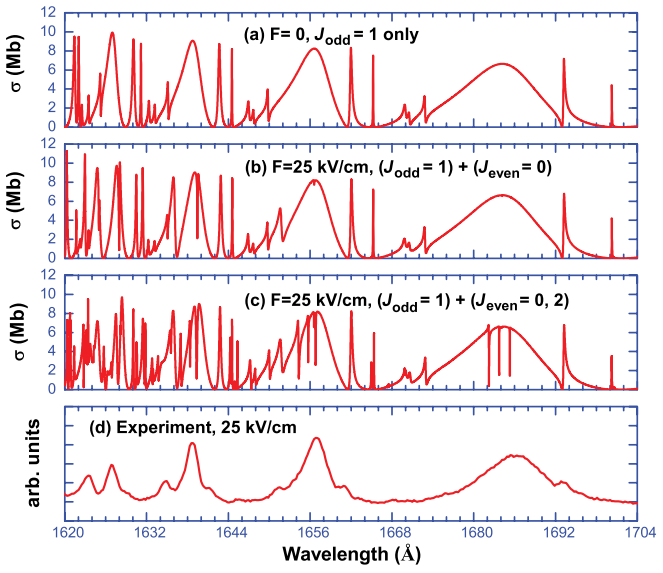

FIG. 4. (Color online) (a) Calculated field-free $J = 1$ spectrum (with odd parity only). (b) Calculated spectrum at 25 kV/cm that includes $J = 1$ (odd-parity) and $J = 0$ (even-parity) components. (c) Calculated spectrum at 25 kV/cm that includes $J = 1$ (odd-parity), $J = 0$ (even-parity), and $J = 2$ (even-parity) components. (d) Observed spectrum at $F = 25$ kV/cm.

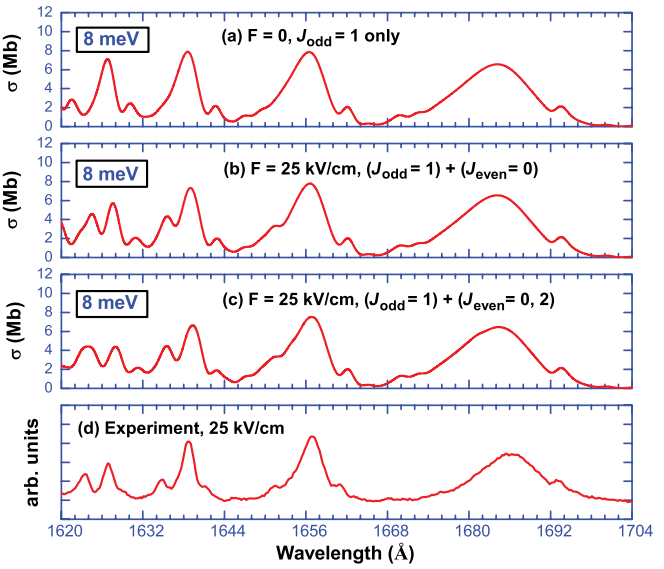

FIG. 5. (Color online) Comparison between (d) the observed spectrum at $F = 25$ kV/cm and (a–c) the convoluted spectra with an 8-meV Gaussian slit function for the three theoretical spectra shown in Figs. 4(a)–4(c).

For a crossing in width, or $\delta\Gamma = 0$, $\Delta\Gamma \to 0$ as $F \to F_o$; that is ,

$$A \simeq (ia_I)^2(F - F_o)^2 + (\Delta E)^2 + 2(ia_I)\Delta E(F - F_o) + (c_R + ic_I) \tag{10}$$

has to be real and positive; that is, $a_I(F - F_o) = -\frac{c_I}{2\Delta E}$. This leads to the necessary condition

$$A = -\left(\frac{c_I}{2\Delta E}\right)^2 + c_R + (\Delta E)^2 > 0. \tag{11}$$

Since V_{ab} is a relatively slow-varying function of F, the energy separation between the two energy levels, that is, $\delta E = \sqrt{A}$, also varies slowly as F increases and does not change sign when F moves from one side of F_o to the other side or lead to an avoided crossing in energy. In other words, one might anticipate a substantial transfer in width (i.e., a crossing)

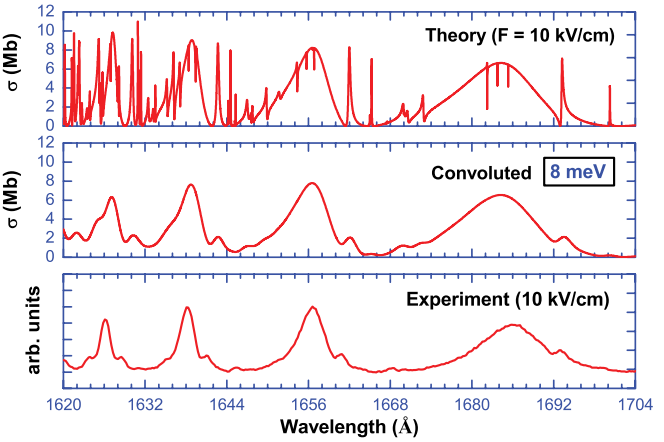

FIG. 6. (Color online) Comparison between theory and experiment at $F = 10$ kV/cm. The theoretical spectrum is convoluted with an 8-meV Gaussian slit function.

between two resonances near an avoided crossing in energy. Similarly, one could show that the necessary condition for a crossing in energy is given by

$$A = \left(\frac{c_I}{\Delta\Gamma}\right)^2 + c_R - \left(\frac{\Delta\Gamma}{2}\right)^2 < 0. \quad (12)$$

This leads to a relatively slow-varying separation in width $\delta\Gamma = -\sqrt{-A}$ with no sign change near F_o. In other words, one should anticipate only minor transfer of width near an actual energy crossing between two resonances.

Figure 3 summarizes the experimentally observed Stark spectra as the field strength increases. Three autoionization series based on the earlier BSCR calculation [16] at zero field are identified to facilitate our discussion. Many of the detailed resonance structures could not easily be identified in the observed spectra either due to the limitation of the experimental energy resolution or because the resonance is "hidden" when it is overshadowed by other, more prominent resonances. The observed spectra, nevertheless, clearly show that they are affected by the field effect, especially on the higher energy side of the $3d8p\ ^1P_1$ resonance. As a result, we focus our more detailed discussion later in this section on the spectral region with wavelengths shorter than 1645 Å.

To study the field-induced structures in detail, a BSCR calculation was carried out for field strengths up 25 kV/cm and beyond, if necessary, for an in-depth analysis of spectra near crossing or avoided crossing of energy between neighboring resonances. Figure 4(a) presents the theoretical spectrum of the field-free ground-state photoionization of Ca with only the $J = 1$ odd-parity components (i.e., $^{1,3}P^o_{J=1}$ and $^3D^o_{J=1}$) included in the final-state function. Figure 4(b) shows a substantial change in the calculated spectrum, at a field strength close to 25 kV/cm, due to Stark mixing of the $J = 1$ odd-parity components (i.e., $^{1,3}P^o_{J=1}$ and $^3D^o_{J=1}$) with the $J = 0$ even-parity components (i.e., $^1S^e_{J=0}$ and $^3P^e_{J=0}$) in the energy region above the $3d8p\ ^1P_1$ resonance (i.e., with a wavelength shorter than 1645 Å). The widths of the dominant $3dnp\ ^1P_1$ ($n = 9$–10) resonances in the field-free spectrum are reduced and their transition amplitudes are transferred in part to their neighboring resonances, with their resonance energies shifted down toward the lower energy side. Our calculated spectrum also leads to a number of narrow window resonances, which superimpose on the broad $3dnp\ ^1P_1$ ($n = 7 - 10$) resonances.

Figure 4(c) presents the theoretical spectrum when all three J components, that is, $^{1,3}P_1$ and $^3D_1$ for $J = 1$, $^1S_0$ and $^3P_0$ for $J = 0$, and $^3P_2$, $^{1,3}D_2$, and $^3F_2$ for $J = 2$, are coupled together by the electric field. Many more Stark-induced structures appear compared with the observed spectrum shown in Fig. 4(d), especially on the shorter wavelength side, where the spectrum is also very different from the field-free one. To better compare our theoretical and experimental results, all three calculated spectra are convoluted with a Gaussian slit function at an experimental energy resolution of 8 meV. Figure 5 shows a good agreement between our experimental and our theoretically convoluted results. With only Stark mixing of the $J = 1$ and $J = 0$ components, the convoluted spectrum already reproduces the observed one up to about 1634 Å very well. Stark mixing due to $J = 2$ components contributes mostly to the shorter wavelength region below

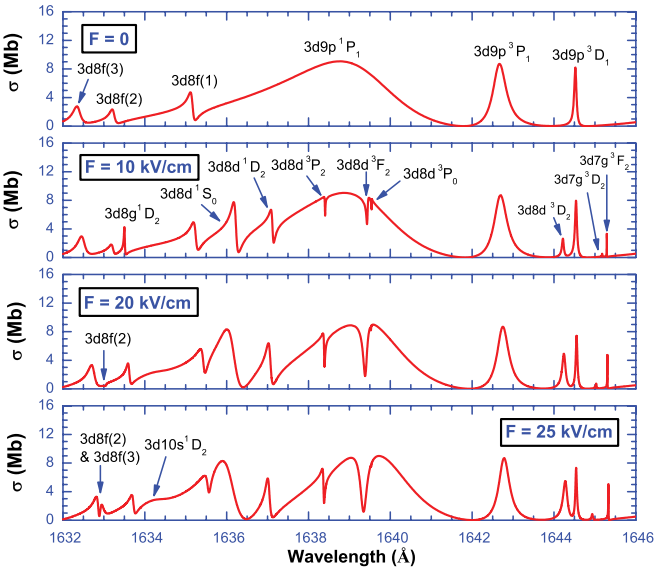

FIG. 7. (Color online) Calculated spectra between 1632 and 1646 Å as the field strength F varies from 0 to 25 kV/cm.

1634 Å. Interestingly, the convoluted theoretical spectrum, Fig. 5(c), shows that near 1685 Å, the three narrow, $J = 2$, even-parity (i.e., $3d6d\ ^1D_2$, $^3P_2$, and $^3F_2$) window-like structures, which are superimposed on the broad $3d7p\ ^1P_1$ resonance shown in Fig. 4(c), have slightly flattened tops. This suggests that the less pointed top of the observed $3d7p\ ^1P_1$ resonance may in fact be a signature of a series of window resonances, instead of being an experimental artifact. Figure 6 compares the theoretically calculated and convoluted spectra with the measured spectra at $F = 10$ kV/cm. The overall agreement between theory and experiment is good, although the detailed structures of many resonances are not resolved in the observed spectra. The difference in our calculated length

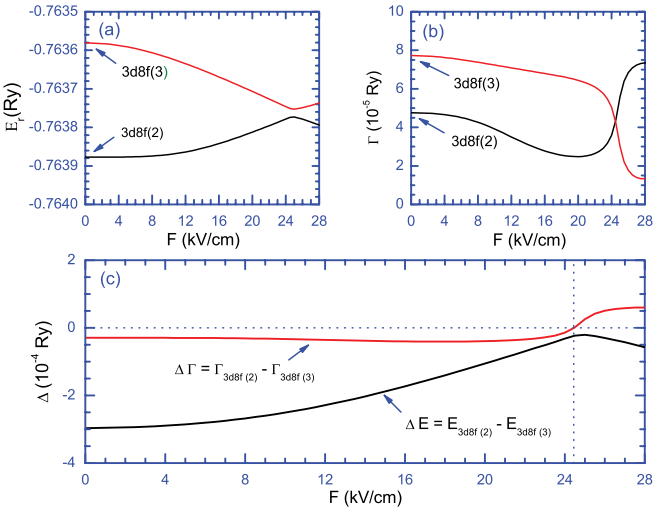

FIG. 8. (Color online) (a,b) A nearly complete exchange (i.e., "crossing") of widths between the $3d8f(2)$ and the $3d8f(3)$ resonances due to a nearly symmetric avoided crossing of energy between these two resonances. (c) When the widths cross near $F =$ 24 kV/cm, the energies of these two interacting resonances do not cross.

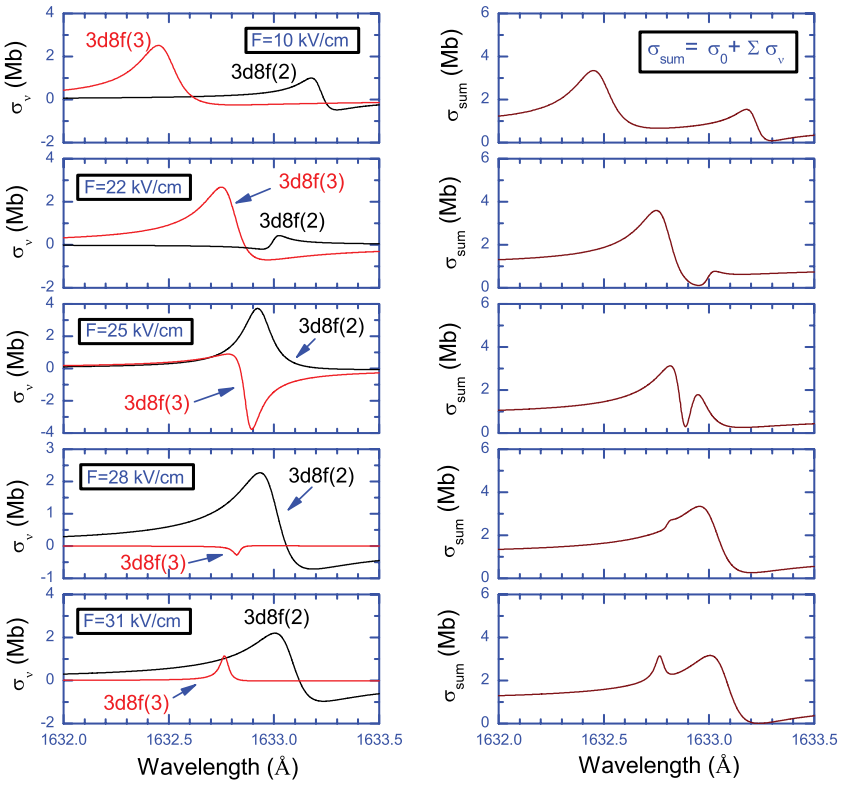

FIG. 9. (Color online) Variation of the individual contributions from the $3d8f(3)$ and $3d8f(2)$ resonances to the total cross sections between 1632 and 1633.5 Å as F increases from 10 to 31 kV/cm.

TABLE I. Calculated resonance energies E_r (in Ry), widths Γ (in $a[n] = a \times 10^n$ Ry), and probability densities ρ_J (in %) of resonances shown in theoretical spectra between 1626.5 and 1632 Å in the presence of external fields F (in kV/cm). Effective quantum numbers ν_0 for each field-free resonance against the $3d$ threshold are also listed.

F	E_r	Γ	ρ_0	ρ_1	ρ_2	E_r	Γ	ρ_0	ρ_1	ρ_2
		$3d10p\,^3D_1$ ($\nu_0 = 8.07$)					$3d9d\,^3P_0$ ($\nu_0 = 8.34$)			
0	−0.763 173	3.01[−5]	0	100	0	−0.762 164	2.98[−7]	100	0	0
10	−0.763 250	1.53[−5]	4	46	50	−0.762 142	3.57[−6]	52	27	21
20	−0.763 345	1.46[−5]	7	42	51	−0.762 133	5.74[−6]	32	32	36
25	−0.763 394	1.41[−5]	7	41	52	−0.762 146	6.38[−6]	29	32	39
		$3d8g\,^3F_2$ ($\nu_0 = 8.07$)					$3d9d\,^3F_2$ ($\nu_0 = 8.37$)			
0	−0.763 162	3.93[−7]	0	0	100	−0.762 086	8.16[−6]	0	0	100
10	−0.763 095	1.04[−5]	4	34	62	−0.762 080	1.23[−5]	12	21	67
20	−0.763 017	1.39[−5]	3	34	63	−0.762 054	1.49[−4]	18	35	47
25	−0.762 972	1.53[−5]	5	35	60	−0.761 954	1.43[−4]	19	34	47
		$3d8g\,^3D_2$ ($\nu_0 = 8.07$)					$3d10p\,^1P_1$ ($\nu_0 = 8.44$)			
0	−0.763 150	1.86[−6]	0	0	100	−0.761 829	6.41[−4]	0	100	0
10	−0.763 129	3.70[−5]	4	33	63	−0.761 894	5.48[−4]	16	55	29
20	−0.763 213	8.06[−5]	11	40	49	−0.762 048	2.88[−4]	20	37	43
25	−0.763 283	9.13[−5]	14	40	46	−0.762 219	2.49[−4]	20	41	39
		$3d9d\,^3D_2$ ($\nu_0 = 8.09$)					$3d9d\,^3P_2$ ($\nu_0 = 8.48$)			
0	−0.763 095	1.08[−5]	0	0	100	−0.761 717	3.20[−6]	0	0	100
10	−0.763 092	8.37[−6]	2	31	67	−0.761 714	7.76[−6]	2	15	83
20	−0.763 000	1.17[−5]	6	38	56	−0.761 704	1.67[−5]	4	23	73
25	−0.762 945	1.79[−5]	7	40	53	−0.761 700	2.13[−5]	4	26	70
		$3d10p\,^3P_1$ ($\nu_0 = 8.16$)								
0	−0.762 803	1.35[−4]	0	100	0					
10	−0.762 814	1.06[−4]	11	60	29					
20	−0.762 807	5.53[−5]	12	48	40					
25	−0.762 789	3.73[−5]	12	45	43					

TABLE II. Calculated resonance energies E_r (in *Ry*), widths Γ (in $a[n] = a \times 10^n$ Ry), and probability densities ρ_J (in %) of resonances shown in theoretical spectra between 1622 and 1626.5 Å in the presence of external fields F (in kV/cm). Effective quantum numbers ν_0 for each field-free resonance against the $3d$ threshold are also listed.

F	E_r	Γ	ρ_0	ρ_1	ρ_2	E_r	Γ	ρ_0	ρ_1	ρ_2
		$3d11s\,^3D_2$ ($\nu_0 = 8.57$)					$3d11s\,^1D_2$ ($\nu_0 = 8.84$)			
0	−0.761 417	1.96[−4]	0	0	100	−0.760 603	2.30[−4]	0	0	100
10	−0.761 427	1.88[−4]	5	25	70	−0.760 606	2.13[−4]	4	30	66
20	−0.761 456	1.43[−4]	8	36	56	−0.760 600	2.01[−4]	10	37	53
25	−0.761 470	1.10[−4]	10	38	52	−0.760 582	2.04[−4]	14	38	48
		$3d9d\,^1D_2$ ($\nu_0 = 8.60$)					$3d9f(2)$ ($\nu_0 = 8.86$)			
0	−0.761 326	1.15[−5]	0	0	100	−0.760 538	3.42[−5]	0	100	0
10	−0.761 310	2.25[−5]	13	15	72	−0.760 529	2.77[−5]	3	53	44
20	−0.761 311	1.50[−5]	19	21	60	−0.760 456	4.00[−5]	9	44	47
25	−0.761 317	1.28[−5]	17	25	58	−0.760 498	5.13[−5]	17	43	40
		$3d9d\,^1S_0$ ($\nu_0 = 8.65$)					$3d9f(3)$ ($\nu_0 = 8.99$)			
0	−0.761 170	8.69[−7]	100	0	0	−0.760 183	5.53[−5]	0	100	0
10	−0.761 163	8.69[−5]	29	44	27	−0.760 259	4.45[−5]	8	56	36
20	−0.761 058	2.37[−4]	28	36	36	−0.760 402	3.47[−5]	13	44	43
25	−0.761 024	2.84[−4]	22	37	41	−0.760 481	1.09[−4]	15	41	44
		$3d9f(1)$ ($\nu_0 = 8.66$)					$3d11p\,^3D_1$ ($\nu_0 = 9.04$)			
0	−0.761 132	3.35[−5]	0	100	0	−0.760 028	5.30[−5]	0	100	0
10	−0.761 154	3.74[−5]	28	44	28	−0.760 127	7.32[−5]	11	52	37
20	−0.761 258	6.81[−5]	11	41	48	−0.760 294	9.26[−5]	15	40	45
25	−0.761 315	8.27[−5]	10	36	54	−0.760 316	2.20[−5]	10	42	48
		$3d9g\,^1D_2$ ($\nu_0 = 8.81$)					$3d10d\,^3D_2$ ($\nu_0 = 9.05$)			
0	−0.760 680	6.58[−7]	0	0	100	−0.760 008	1.31[−5]	0	0	100
10	−0.760 670	1.48[−5]	3	43	54	−0.760 076	2.82[−5]	5	40	55
20	−0.760 741	2.17[−5]	7	50	43	−0.760 228	1.21[−5]	4	43	53
25	−0.760 793	1.60[−5]	8	49	43	−0.760 275	1.60[−5]	12	39	49

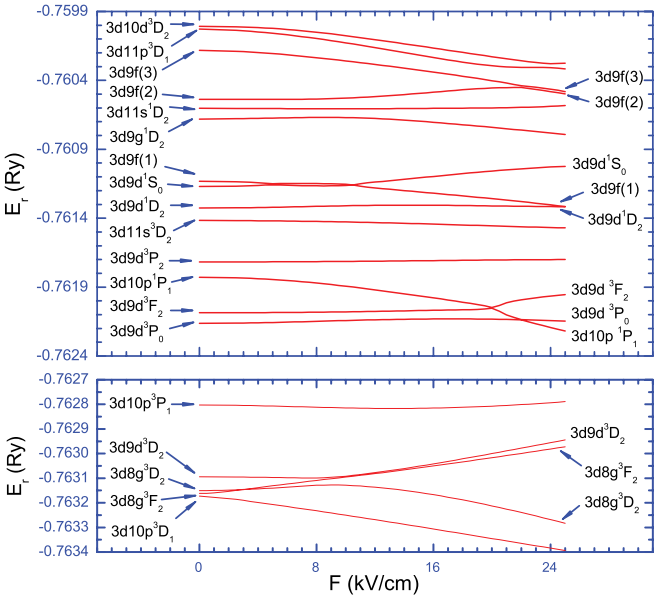

FIG. 10. (Color online) Energy variation for resonances between $3d10d\,^3D_2$ and $3d10p\,^3D_1$ as F increases from 0 to 25 kV/cm.

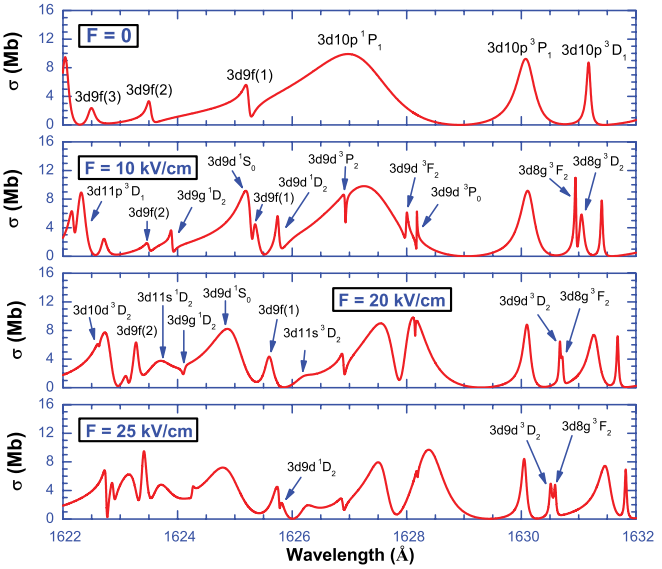

FIG. 11. (Color online) Calculated spectra between 1622 and 1632 Å as the field strength F varies from 0 to 25 kV/cm.

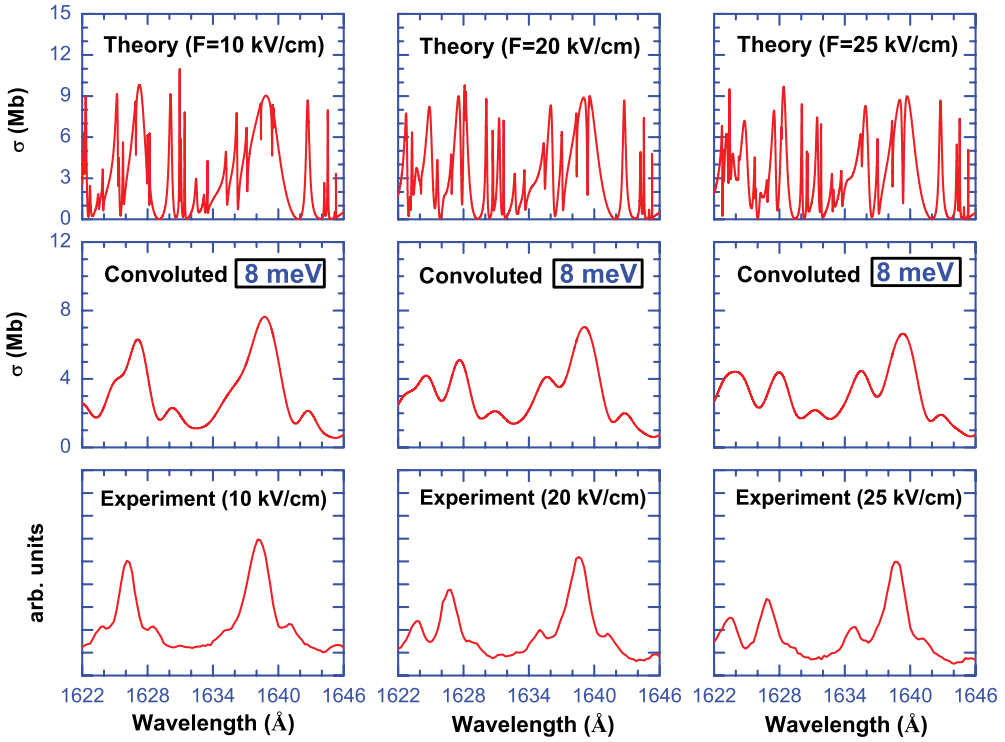

FIG. 12. (Color online) Calculated, convoluted, and observed spectra at $F = 10$, 20, and 25 kV/cm between 1622 and 1646 Å.

versus velocity results is generally about 5%–8% or less. Only the length results are shown.

In the energy region near the $3d9p\ ^1P_1$ resonance, the field effect is clearly evident as shown in Fig. 7. In addition to the even-parity $3d8d\ ^1S_0$, $^1D_2$, $^3P_2$, $^3F_2$, $^3P_0$, and $^3D_2$ resonances, two narrow resonances, $3d8g\ ^1D_2$ and $3d7g\ ^3F_2$, are clearly visible in the theoretical spectrum even at a relatively weak $F = 10$ kV/cm. As F increases, the $3d7g\ ^3D_2$ resonance shows up as a tiny peak on the longer wavelength side of the $3d9p\ ^3D_1$ resonance. In addition, the $3d10s\ ^1D_2$ resonance appears as a hump close to 1634.2 Å, between the $3d8f(1)$ and the $3d8g\ ^1D_2$ resonances. Other resonances, such as $3d10s\ ^3D_2$,

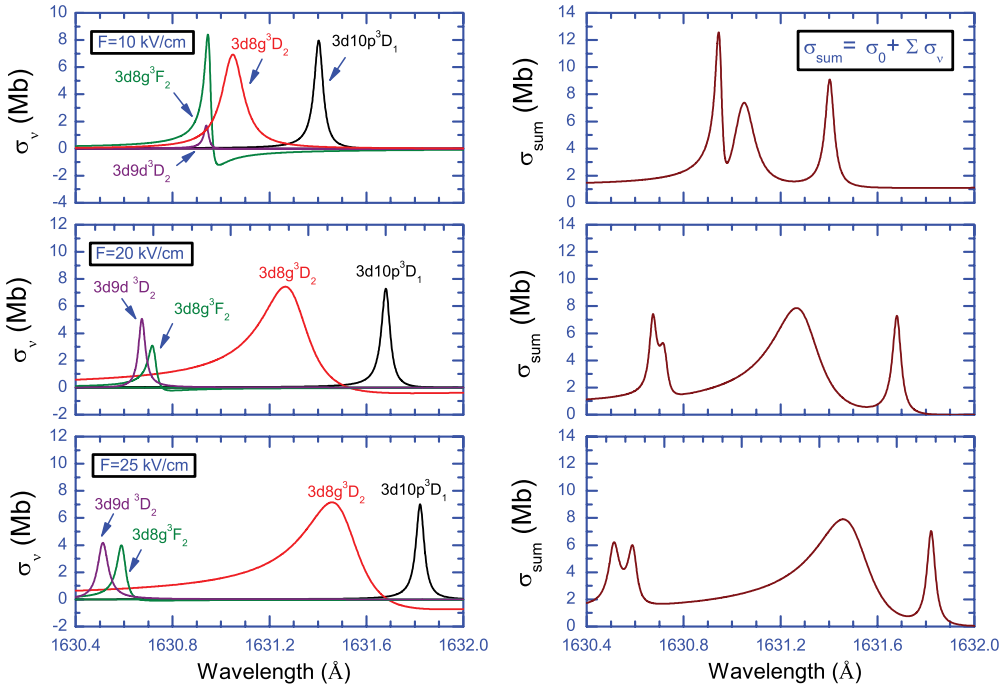

FIG. 13. (Color online) Variation of the individual contributions from four resonances to the total cross sections between 1630.4 and 1632 Å as F increases from 10 to 25 kV/cm.

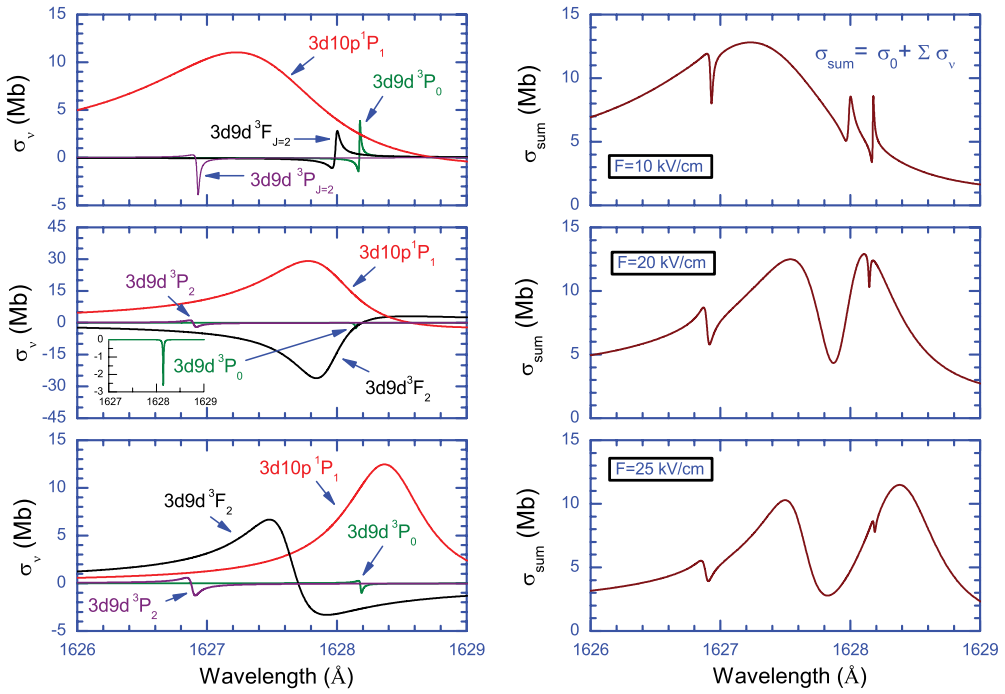

FIG. 14. (Color online) Variation of the individual contributions from four resonances to the total cross sections between 1626 and 1629 Å as F increases from 10 to 25 kV/cm.

near 1636.6 Å, are still too weak to be identified. As F increases further, the $3d8d\,^3P_0$ resonance no longer appears in the spectrum, as it is "hidden" in the dip of the window-like $3d8d\,^3F_2$ resonance near 1639.4 Å. Similar to what we found for states at zero field [16], the mixing of the spin states for the $J = 1$ $3dnf$ multiplets due to the spin-orbit interaction remains strong and one could not assign a total spin for those states. Accordingly, they are labeled numerically as $3dnf(1)$, $3dnf(2)$, and $3dnf(3)$ as we did earlier.

Following the discussion presented earlier, as F increases, our calculation leads to an exchange of the widths (i.e., the actual crossing of width shown in Fig. 8) between the $3d8f(3)$ and the $3d8f(2)$ resonances due to the avoided crossing of energy between these two resonances near 25 kV/cm. We are also able to examine in detail the contribution to the total cross section of individual resonances, based on the procedure outlined in [10]. Figure 9 shows the variation in individual contributions of the two neighboring $3d8f(3)$ and $3d8f(2)$

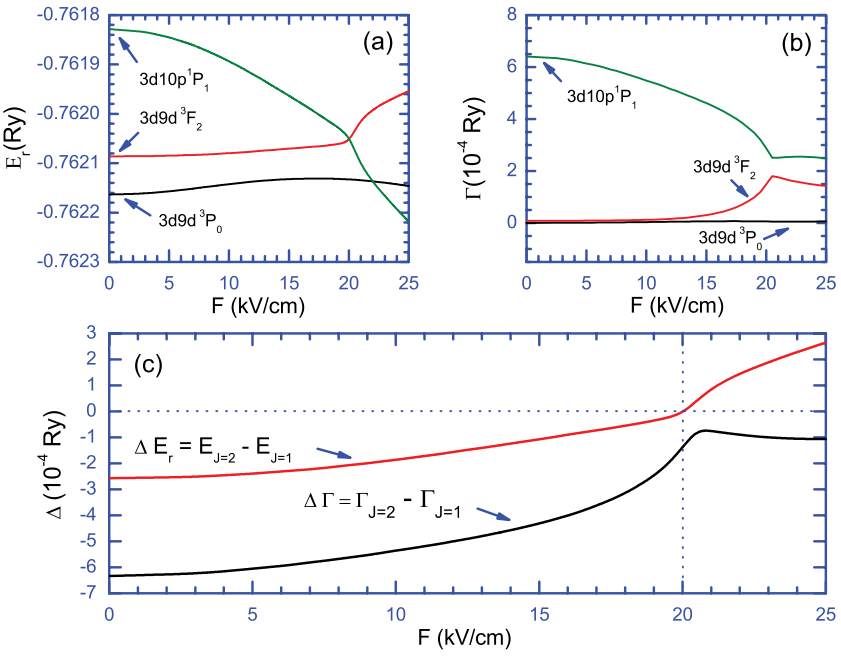

FIG. 15. (Color online) (a) Energy crossings between the broad $3d10p\,^1P_1$ resonance and two neighboring resonances, $3d9d\,^3F_2$ and $3d9d\,^3P_0$, as F varies. (b) Their corresponding variation in widths. (c) When the energies of the $3d10p\,^1P_1$ and $3d9d\,^3F_2$ resonances cross near $F = 20$ kV/cm, the widths of these two interacting resonances do not cross.

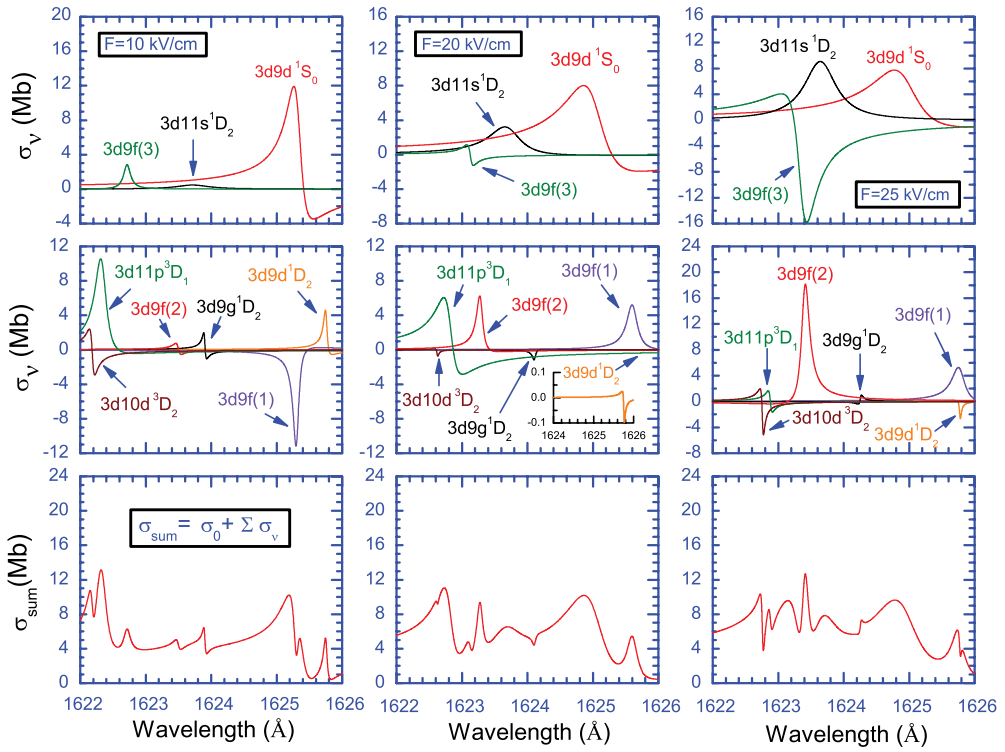

FIG. 16. (Color online) (Color online) Variation of the individual contributions from nine resonances to the total cross sections between 1622 and 1626 Å as F increases from 10 to 25 kV/cm.

resonances (from the plots on the left hand side) to the total cross section (from the plots on the right-hand side) as F increases up to 31 kV/cm. We should note that the individual contribution from each resonance may be negative since it does not include the background cross section. The total cross section plotted on the right hand side of Fig. 9 is always positive, as it should be, when the background cross section is included. Our calculation shows clearly an increase in width for the $3d8f(2)$ resonance while the width of the $3d8f(3)$ resonance decreases due to the avoided crossing of energy shown in Fig. 8. At 25 kV/cm, the $3d8f(3)$ resonance appears with a window-like profile (see from Fig. 7 or the plot on the right hand side of Fig. 9) near the center of the more symmetric $3d8f(2)$ resonance.

Tables I and II present the variation of resonance energies and widths as F (in kV/cm) increases for resonances between 1622 and 1632 Å. J mixing, expressed in terms of ρ_J, or the square of the coefficient in Eq. (7), increases substantially as F increases. Figure 10 presents the more detailed energy variation as F increases from 0 to 25 kV/cm for resonances listed in Tables I and II between the $3d10d\ ^3D_2$ and the $3d10p\ ^3D_1$ levels. The corresponding theoretical spectra between 1622 and 1632 Å, shown in Fig. 11, reveal a more prominent field effect on the resonance structure. Figure 12 compares the calculated, the convoluted, and the observed spectra at $F = 10$, 20, and 25 kV/cm on a more refined energy scale between 1622 and 1646 Å. Similar to that in Fig. 9, Fig. 13 shows a detailed analysis of the individual contributions to the total cross section between 1630.4 and 1632 Å. Part of the field-free width of the $3d10p\ ^3D_1$ resonance is lost to its neighboring $J = 2$ resonances as it moves closer to 1632 Å at 25 kV/cm. At 10 kV/cm, the $3d9d\ ^3D_2$ resonance is overshadowed by a near-degenerate $3d8g\ ^3F_2$ resonance and disappears completely from the calculated spectrum. As F increases further, the $3d9d\ ^3D_2$ resonance reappears on the shorter wavelength side of the $3d8g\ ^3F_2$ resonance, whereas both resonances move away to the shorter wavelength side of the $3d8g\ ^3D_2$ resonance, as expected from their energy variation shown in Fig. 10.

The structure profile of the dominating $3d10p\ ^1P_1$ resonance, shown in Fig. 11, varies substantially as F increases. We note with interest that, unlike the window-like $3d9d\ ^3P_2$ resonance, which stays on the shorter wavelength side of

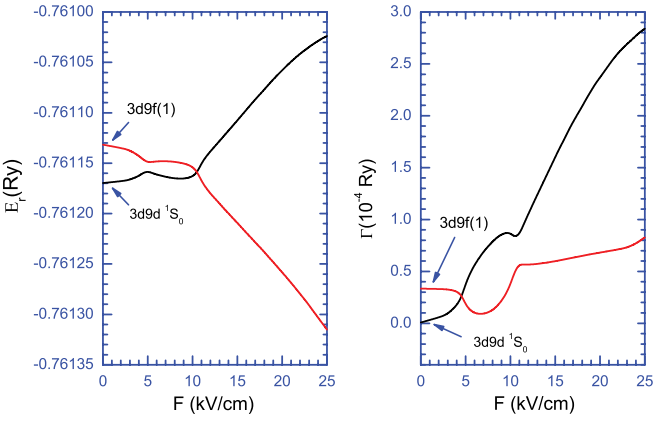

FIG. 17. (Color online) An avoided crossing and a subsequent crossing of energy between the $3d9f(1)$ and the $3d9d\ ^1S_0$ resonances and their corresponding variation in widths as F increases.

the broad $3d10p\ ^1P_1$ resonance, the structure profiles of the $3d9d\ ^3F_2$ and $3d9d\ ^3P_0$ resonances on its longer wavelength side change completely as the field strength F increases. Similar to what is shown in Fig. 13, the three plots on the left in Fig. 14 show a strong variation in the structure profile of the $3d9d\ ^3F_2$ resonance, that is, from an asymmetric profile of negative q parameter at 10 kV/cm to a window-like resonance of near-zero q at 20 kV/cm with a substantial increase in width and, finally, to an asymmetric profile of positive q at 25 kV/cm when it moves across the $3d10p\ ^1P_1$ resonance from the longer wavelength side to the shorter wavelength side. In addition to the variation in the q parameter for the $3d9d\ ^3F_2$ resonance, the resulting structure profiles plotted on the right in Fig. 14 are also strongly affected by the level crossing of energy near 20 kV/cm. The change in the $3d9d\ ^3F_2$ resonance width can be linked directly to the crossing of energy and the corresponding avoided crossing of width between the $3d10p\ ^1P_1$ and the $3d9d\ ^3F_2$ resonances shown in Fig. 15. The presence of the $3d9d\ ^3P_0$ resonance is minimal and barely visible in the spectrum shown. However, a detailed look at the individual contribution to the resonance structure shows that its q parameter also changes sign when it moves across the broad $3d10p\ ^1P_1$ resonance to the shorter wavelength side. The sign change of the q parameter could be attributed to the change from constructive to destructive (or destructive to constructive) interference between the bound-bound contribution and the bound-continuum contribution when the bound-continuum contribution changes sign due to the change of π in its effective scattering phase shift when the energy of a resonance moves upward across another resonance (see, e.g., Fig. 13 in [18]). Such a sign change of the q parameter along an autoionization series, due to a similar sign change resulting from the increase in π when the scattering phase shift moves across a resonance of another overlapping autoionzation series, has been discussed elsewhere [19]. At 25 kV/cm, the tiny peak near 1625.8 Å between the $3d9f(1)$ and the $3d11s\ ^3D_2$ resonances, shown in Fig. 11, is identified as the $3d9d\ ^1D_2$ resonance, according to our BSCR calculation.

We now turn our attention to the spectral region between 1622 Å and 1626 Å, which covers nine resonances from our calculation. Figure 16 presents in detail the individual contribution from these nine resonances at three field strengths.

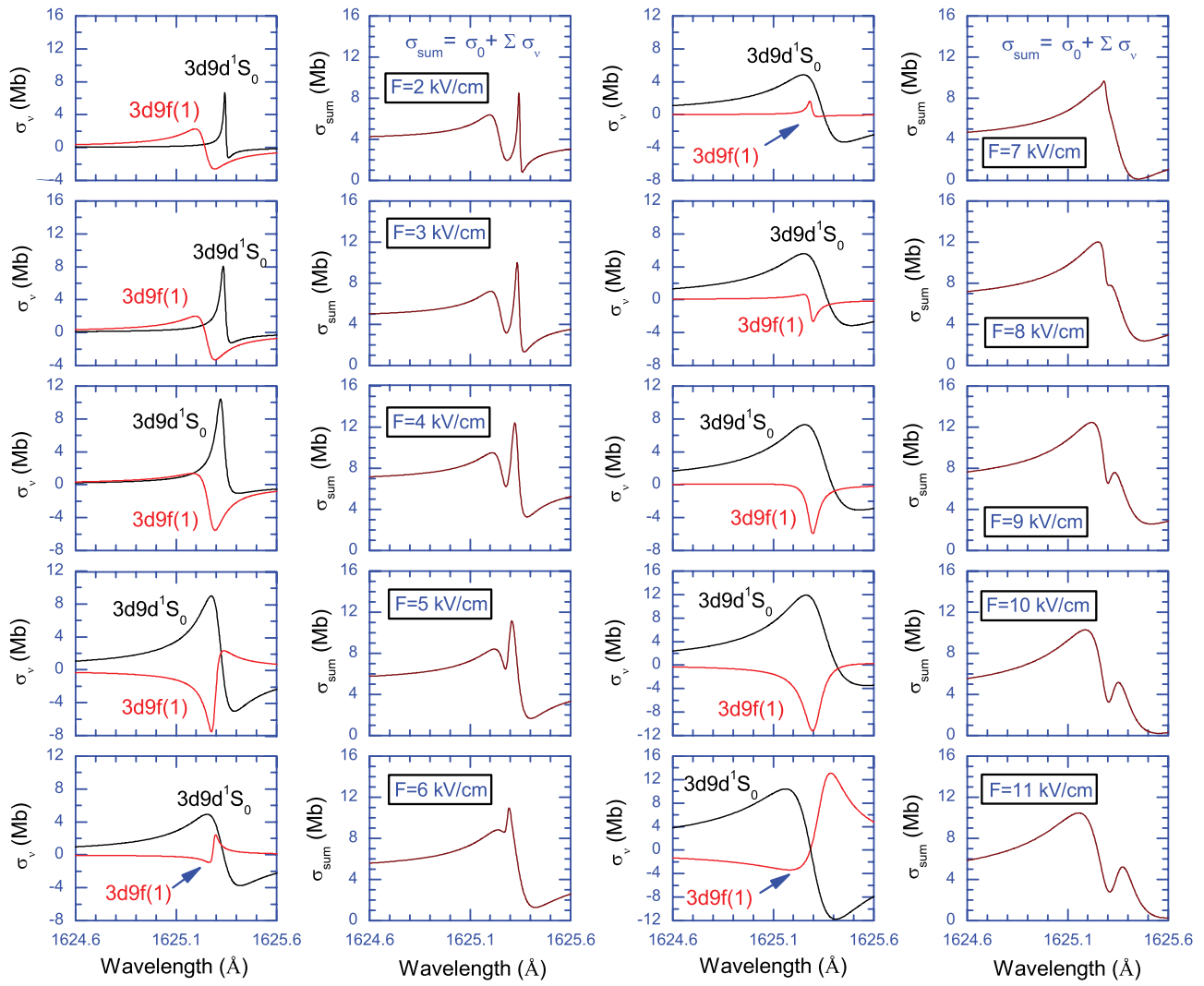

FIG. 18. (Color online) Variation of the individual contributions from the $3d9f(1)$ and $3d9d\ ^1S_0$ resonances to the total cross sections between 1624.6 and 1625.6 Å as F increases from 2 to 11 kV/cm.

The structure profiles of the two closely spaced resonances, $3d10d\,^3D_2$ and $3d11p\,^3D_1$ on the shorter wavelength side, vary substantially as F increases while losing most of their strength to other resonances at 25 kV/cm. Slightly below in energy, shown in Fig. 10, a pair of $J = 1$ resonances, $3d9f(3)$ and $3d9f(2)$, move closer in energy to each other as F increases. Figure 16 shows a considerable change in the structure profiles of these two nearly degenerate resonances at a field strength above 20 kV/cm. At a field strength between 3 and 12 kV/cm, our calculation led to an interesting example of field-induced energy variation between the $3d9f(1)$ and the $3d9d\,^1S_0$ resonances, shown in Fig. 17. We find first an avoided crossing of energy near 5 kV/cm and then a crossing near 10 kV/cm. The variations in width for these two neighboring resonances follow the qualitative feature we pointed out first in this section, that is, the pairing of the avoided crossing of energy and the crossing of width, and vice versa. The individual contributions to the total cross section from these two resonances are shown in detail, from 2 to 11 kV/cm, in Fig. 18. Again, the spectral profiles vary substantially as F increases, while the widths of both resonances increase as shown in Fig. 17. It is interesting to note that the crossing of energy has also led to a sign change of the q parameter of the $3d9f(1)$ resonance (see, e.g., the profiles at 2 and 11 kV/cm) as it moves down in energy across the $3d9d\,^1S_0$ resonance. This is consistent with the sign change of the q parameters for the $3d9d\,^3F_2$ and $3d9d\,^3P_0$ resonances shown in Figs. 14 and 15 when a narrower resonance moves across a broader resonance in energy. Although we find no sign change in the q parameter for a resonance near the avoided crossing of energy, our calculation shows a strong effect on the q parameter due to the substantial overlap between the two resonances. Qualitatively, the transition matrix does not go through a 0 due to a change of π in the scattering phase shift, which happens when there is an actual energy crossing. It, nevertheless, leads to a near-zero value in transition matrix due to a large change in the scattering phase shift and, consequently, a window-like structure profile. The profiles of individual contributions from the $3d8f(3)$ resonance at 25 kV/cm shown in Fig. 9 and the $3d9f(1)$ resonance at 4–5 kV/cm shown in Fig. 18 are two such examples.

In conclusion, as we have shown with a number of examples, the field-induced spectrum is strongly affected by two key qualitative features that dictate the variation of the structure profiles as the field strength F increases. First, near an avoided crossing of energy between two neighboring resonances, the difference in their resonance widths changes sign; that is, a crossing of width leads to a large transfer in width and, thus, a substantial variation in resonance structure profile. Second, near an actual crossing of energy, the sign of the difference in widths stays the same; that is, an avoided crossing of width in itself does not affect significantly the structure profile. However, the q parameter corresponding to the structure profile of an individual resonance changes sign due to the change in interference (from constructive to destructive, or vice versa) between the bound-bound and the bound-continuum contributions to the transition amplitude for a narrow resonance as it moves across a broader resonance in energy as F varies. This change in the q parameter again leads to a large variation in the resonance structure profile. Based on our detailed theoretical calculation, we are also able to assign nominally some of the resonances in terms of their field-free symmetries (i.e., the parity, the total spin S, the total orbital angular momentum L, and the total angular momentum J). It is clear, however, that all these symmetries are broken in the presence of strong mixing due to the spin-dependent interactions as well as the external field.

ACKNOWLEDGMENTS

This work was supported by the National Science Council in Taiwan under Grants no. NSC 96-2112-M-008-010-MY3, NSC 97-2112-M-030-002, and NSC 99-2119-M-007-001.

[1] M. G. Littman, M. L. Zimmerman, and D. Kleppner, Phys. Rev. Lett. **37**, 486 (1976).
[2] M. L. Zimmerman, M. G. Littman, M. M. Kash, and D. Kleppner, Phys. Rev. A **20**, 2251 (1979).
[3] M. L. Zimmerman, T. W. Ducas, M. G. Littman, and D. Kleppner, J. Phys. B **11**, L11 (1978).
[4] K. A. Safinya, J. F. Delpech, and T. F. Gallagher, Phys. Rev. A **22**, 1062 (1980); R. R. Jones and T. F. Gallagher, *ibid.* **39**, 4583 (1989).
[5] V. L. Jacobs and J. Davis, Phys. Rev. A **19**, 776 (1979); V. L. Jacobs, J. Davis, and P. C. Kepple, Phys. Rev. Lett. **37**, 1390 (1976).
[6] B. E. Cole, J. W. Cooper, and E. B. Saloman, Phys. Rev. Lett. **45**, 887 (1980); J. W. Cooper and E. B. Saloman, Phys. Rev. A **26**, 1452 (1982).
[7] R. R. Freeman and G. C. Bjorklund, Phys. Rev. Lett. **40**, 118 (1978).
[8] D. J. Armstrong and C. H. Greene, Phys. Rev. A **50**, 4956 (1994).
[9] T. K. Fang and Y. K. Ho, Phys. Rev. A **60**, 2145 (1999); K. T. Chung, T. K. Fang, and Y. K. Ho, J. Phys. B **34**, 165 (2001).
[10] T. K. Fang and K. T. Chung, J. Phys. B **34**, 1245 (2001).
[11] J. R. Harries, J. P. Sullivan, J. B. Sternberg, S. Obara, T. Suzuki, P. Hammond, J. Bozek, N. Berrah, M. Halka, and Y. Azuma, Phys. Rev. Lett. **90**, 133002 (2003).
[12] X. M. Tong and C. D. Lin, Phys. Rev. Lett. **92**, 223003 (2004).
[13] A. Mihelič and M. Zitnik, Phys. Rev. Lett. **98**, 243002 (2007).
[14] I. A. Ivanov and Y. K. Ho, Phys. Rev. A **68**, 033410 (2003).
[15] T. K. Fang and T. N. Chang, Phys. Rev. A **76**, 012721 (2007).
[16] J. H. Chen, T. K. Fang, C. C. Chu, T. S. Yih, and T. N. Chang, Phys. Rev. A **80**, 042509 (2009).
[17] T. N. Chang, in *Many-Body Theory of Atomic Structure and Photoionization*, edited by T. N. Chang (World Scientific, Singapore, 1993), p. 213.
[18] T. N. Chang and T. K. Fang, Radiat. Phys. Chem. **70**, 173 (2004).
[19] T. K. Fang and T. N. Chang, Phys. Rev. A **61**, 052716 (2000).